Green Chemistry

PAPER

View Article Online
View Journal

Cite this: DOI: 10.1039/d5gc02044a

Quenching-triggered amorphous/crystalline-heterostructure with tensile strain achieves efficient alkaline HER kinetics by operating the unique Co_1–P–Co_2 electrocatalytic mechanism†

Yunmei Du, ‡[a,b] Jinghan Xu,‡[a,c] Shan Lu,[a,b] Zhenyu Xiao, [a,c] Yanru Liu,[a,c] Kang Liu [a,c] and Lei Wang *[a,c]

Received 23rd April 2025,
Accepted 7th July 2025

DOI: 10.1039/d5gc02044a

rsc.li/greenchem

Finding a feasible technique to introduce strain into phosphides to achieve Pt-like performance in the hydrogen evolution reaction (HER) is a challenge. This work innovatively adopted phosphorization–quenching technology to successfully construct CoOx/CoP-L nanosheets with an amorphous/crystalline (a/c)-heterostructure and 2.65% tensile strain. Strikingly, quenching also triggered a distorted lattice structure, promoting the exposure of active sites. Surprisingly, the well-designed CoOx/CoP-L needs only 56.6 mV and 98 mV to drive a current density of 10 mA cm^{-2} for alkaline and acidic HER, respectively. Especially for alkaline HER, its performance exceeds that of Pt/C at high current density. Overall, this work provides a new design idea for transition-metal-based catalysts to optimize the catalytic mechanism of alkaline HER and achieve a performance surpassing that of Pt.

Green foundation

1. CoOx/CoP-L with a crystalline/amorphous-heterostructure and 2.65% tensile strain was obtained by a facile phosphorization–quenching strategy, achieving low-energy consumption and high-efficiency hydrogen production, in accord with the principles of Green Chemistry for the utilization of renewable resources.
2. CoOx/CoP-L exhibits superior performance and ultra-high stability compared to Pt/C in the alkaline HER process, laying the foundation for further industrial applications.
3. This work innovatively induced an a/c-heterostructure and lattice strain in phosphides through a quick-freezing strategy, and made a big step towards realizing the exceptional HER activity of phosphides beyond Pt and industrial applications. To enhance environmental sustainability, future studies could optimize the synthesis to reduce energy consumption and potential waste. Further enhancing the long-term stability and recyclability of the catalysts would contribute to even greener catalytic oxidation processes.

1. Introduction

With proposals and advocacy for a "dual carbon" target strategy, the adjustment of the energy structure is imminent, requiring the vigorous development of clean, renewable, and environmentally friendly alternative energy.[1–4] Hydrogen energy has become a hot topic in the global search for an ideal energy source.[5–8] Transition metal phosphides (TMPs), due to their characteristics of a hydrogenase-like catalytic mechanism and low cost, have satisfying prospects for the hydrogen evolution reaction (HER).[9–12] However, their real catalytic activity is far from comparable to that of Pt-based catalysts.[13–15] Therefore, activating the active sites of bulk TMPs to achieve HER performance beyond that of Pt is an important challenge.

As an effective strategy to improve the electrocatalytic performance from the kinetic level,[16–18] strain engineering fundamentally promotes the adsorption/desorption of reaction intermediates and the exposure of more highly active sites by precisely regulating the electronic structure, d-band center, and lattice distortion.[19–21] Notably, chemical ways of introducing strain, like doping or grain boundary mismatch, also change

[a]Cultivation Base of Ecological Chemical Industry Key Laboratory, International Science and Technology Cooperation Base of Eco-chemical Engineering and Green Manufacturing, Qingdao University of Science and Technology, Qingdao 266042, P. R. China. E-mail: inorgxiaozhenyu@163.com, inorchemwl@126.com
[b]College of Environment and Safety Engineering, Qingdao University of Science and Technology, Qingdao 266042, P. R. China
[c]College of Chemistry and Molecular Engineering, Qingdao University of Science and Technology, Qingdao 266042, P. R. China

†Electronic supplementary information (ESI) available. See DOI: https://doi.org/10.1039/d5gc02044a

‡These authors contributed equally.

the material's structure and composition, which makes it hard to identify the true source of catalytic activity. Furthermore, methods of preparing strained structures mostly involve complex synthesis processes, expensive equipment, or cumbersome post-treatment processes (ion exchange, etching, calcination, *etc.*), hampering their use in large-scale industrial applications.[22,23] Therefore, designing TMPs with a strained structure and enhanced reaction kinetics by a rapid, low energy, and universal strategy will be of great value, but it is still challenging.

As a non-equilibrium thermochemical reaction, quenching technology has the characteristics of simple operation, lower time-consumption, low-energy consumption, and green environmental protection, showing great application potential in the directional construction of catalysts and industrial-scale production.[24–26] Interestingly, Shen, Guan, and Bajdich *et al.* confirmed that rapid quenching of transition-metal-based oxides (or alloys) directly induced the lattice to produce compressive strain[27,28] and tensile strain[29,30] and then optimized its electronic structure and electrocatalytic kinetics. Meanwhile, Hu's group also pointed out that quenching treatment can lead to a large number of dislocations on the surface of Pt particles and IrNi alloys, inducing a lattice strain effect.[31,32] Moreover, Zhang *et al.* introduced different degrees of tensile strain in MoS_2 by heat-quenching treatment, promoting more electrons to occupy the bonding orbitals to weaken the Li–S and S–S bonds.[33] In summary, quenching technology shows great potential for application in inducing strain structure in oxides or alloys.[34,35] However, the use of quenching technology to regulate strain structures in TMPs with promising applications remains underexplored. In addition, the real mechanism of influence of quenching-induced strain structure on the electrocatalytic performance of TMPs needs to be further clarified.

Based on the above considerations, CoOx/CoP-L nanosheets with an amorphous/crystalline (a/c)-heterostructure and 2.65% tensile strain were creatively constructed by the 'phosphorization–liquid nitrogen quenching' treatment of amorphous CoOx nanosheets. Moreover, liquid nitrogen quenching also triggered distortion of the lattice structure, facilitating the exposure of active sites. Density functional theory (DFT) calculations and *in situ* Raman results confirm that construction of the a/c-CoOx/CoP heterostructure with 2.65% tensile strain optimizes the energy barrier to H^+ adsorption for acid HER and water adsorption–dissociation for alkaline HER. Strikingly, the a/c-CoOx/CoP heterostructure with 2.65% tensile strain creates a unique electrocatalytic pathway for alkaline HER. Strikingly, a unique Co_1–P–Co_2 electrocatalytic pathway for alkaline HER is innovatively proposed for the a/c-CoOx/CoP heterostructure with 2.65% tensile strain. Among the sites, the Co_1 site at the a/c-heterointerface and the Co_2 site at the amorphous CoOx are a hydrophilic site and site for the adsorption of OH^-, respectively, effectively avoiding poisoning of the hydrophilic site and accelerating the alkaline HER kinetics. As anticipated, the well-designed CoOx/CoP-L nanosheets require ultra-low overpotentials of only 128.1 mV and 163.6 mV to drive 100 mA cm^{-2} for alkaline and acidic HER, which is significantly better than for most developed non-noble–metal-based catalysts. Overall, this work introduces an innovative quick-freezing strategy to induce the a/c-heterostructure and lattice strain in phosphides, marking a significant step towards achieving exceptional HER activity surpassing that Pt and advancing their industrial application.

2. Experimental section

2.1. Ultrathin CoOx nanosheets

145.5 mg of $Co(NO_3)_2{\cdot}6H_2O$ and 0.91 g of CTAB were sonicated in 20 mL of deionized water, denoted solution A. Solution A was sonicated in deionized water. 47.29 mg of $NaBH_4$ was dissolved in 5 mL of deionized water to prepare solution B. Solution B was added dropwise to the stirred solution A, then the mixture was stirred for 12 h, centrifuged, and washed several times with deionized water.

2.2. CoOx/CoP-L

0.6 g of sodium hypophosphite and 20 mg of CoOx nanosheets were placed upstream and downstream of the tube furnace, respectively. The tube furnace was then heated to 300 °C. After heating for 1 h, the product was quickly poured into a beaker containing 50 mL of liquid nitrogen and cooled for 10 min. Finally, the cooled product was placed in a vacuum drying oven at 30 °C for use as CoOx/CoP-L.

2.3. Other comparison samples

The products obtained by replacing liquid nitrogen with dry ice and ice water were recorded as CoOx/CoP-D and CoOx/CoP-I, respectively. The sample obtained by natural cooling after phosphatization is CoOx/CoP.

At the same time, the amount of sodium hypophosphite was also adjusted in this work. The samples obtained with 0.2 g and 1 g of sodium hypophosphite were named CoOx/CoP-10-L and CoOx/CoP-50-L, respectively.

3. Results and discussion

The ordinary amorphous-CoOx/crystalline-CoP model (CoOx/CoP), the amorphous-CoOx/crystalline-CoP model with 2.65% tensile strain (CoOx/CoP-L) and the pure crystalline CoP model with 2.65% tensile strain (CoP-L) were constructed and are shown in Fig. 1a. As shown in Fig. 1b and Table S1,† the Gibbs free energies of adsorbing H* (ΔG_{H^*}) in the CoOx/CoP-L and CoOx/CoP models are 0.201 eV and 0.507 eV, respectively, implying that the tensile strain structure accelerates H* adsorption on the CoOx/CoP-L model. In particular, the ultrahigh ΔG_{H^*} value of CoP-L (0.630 eV) implies the importance of the construction of the a/c-heterostructure to enhance the H* binding ability. Generally speaking, the alkaline HER process includes the following steps: adsorption of H_2O molecules, dissociation of H_2O molecules ($^*H_2 \rightarrow {}^*H\text{–}OH$), adsorption of

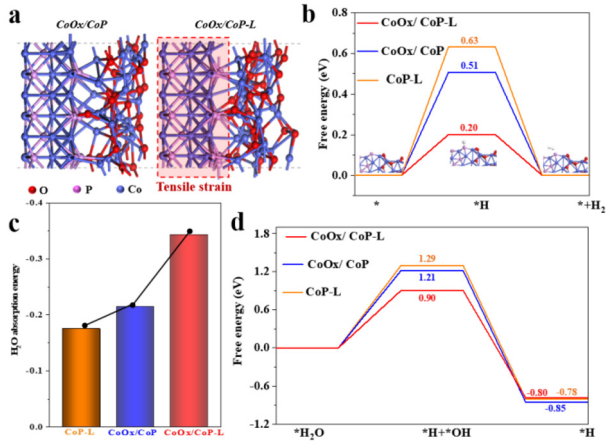

Fig. 1 (a) Theoretical models of CoOx/CoP and CoOx/CoP-L, (b) calculated free energy diagrams of the acid HER pathway, (c) water adsorption energy diagram, and (d) calculated free energy diagrams of the alkaline HER pathway.

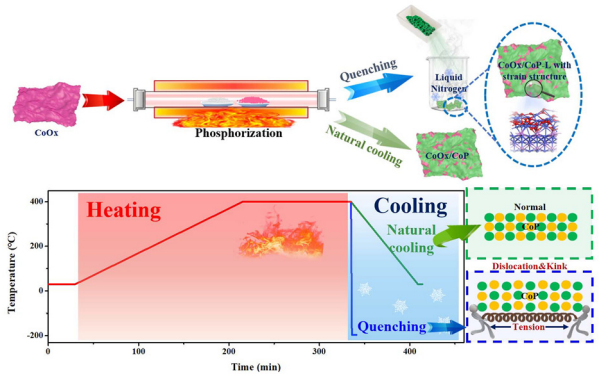

Scheme 1 Synthesis schematic of the CoOx/CoP nanosheets and the CoOx/CoP-L with strain structure.

hydrogen (*H–OH → *H), and escape of hydrogen. Obviously, Fig. 1c and Table S2† show that the adsorption energies of H_2O on the CoP-L and CoOx/CoP-L models are −0.18 and −0.34 eV, respectively, indicating that the amorphous CoOx and the crystalline CoP synergistically promote the adsorption of water molecules. Moreover, the difference (0.11 eV) in hydrophilicity between the CoOx/CoP and CoOx/CoP-L models indicates that the strain structure significantly enhances the water absorption capacity of the well-designed CoOx/CoP-L model, which is a prerequisite for faster alkaline HER kinetics. Notably, Fig. 1d and Table S3† show that the H_2O dissociation process is the rate-determining step of the above models in alkaline HER. The H_2O dissociation barrier of CoOx/CoP-L (0.90 eV) is lower than that of CoOx/CoP (1.21 eV), manifesting that the strain structure effectively reduces the energy barrier to water dissociation and fundamentally accelerates the alkaline HER kinetics. Generally, the construction of the amorphous/crystalline-CoOx/CoP heterostructure and the 2.65% tensile strain synergistically accelerate the HER kinetics by optimizing the energy barriers to H^+ adsorption for acid HER and to water adsorption–dissociation for alkaline HER.

Under the guidance of the above DFT models, Scheme 1 shows that CoOx/CoP and CoOx/CoP-L nanosheets consisting of amorphous CoOx and crystalline CoP were prepared by gas-phase phosphorization. Strikingly, the directional construction of strain structures in phosphides is achieved by regulating the cooling process. Specifically, natural cooling treatment yields CoOx/CoP materials with a normal CoP crystal structure. In contrast, the huge temperature difference generated by the liquid nitrogen (−196 °C) quenching induces a tensile strain in CoP with minor kinks and dislocations, culminating in the formation of the well-defined CoOx/CoP-L catalyst.

As can be seen in Fig. S1 and S2,† the CoOx precursor has an amorphous nanosheet structure, and its thickness is only about 1 nm. To further explore the effect of cooling treatment on the structure of phosphide, the normal CoOx/CoP nanosheets prepared by natural cooling and the well-constructed CoOx/CoP-L prepared by liquid nitrogen quenching were carefully monitored. As can be seen in Fig. S3a,† CoOx/CoP maintains the shape of the nanosheets. However, its thickness in Fig. S4† is significantly greater (~2 nm) than that of the original CoOx precursor. Meanwhile, the HRTEM image in Fig. S3b† confirms the presence of amorphous CoOx (marked by yellow dashed circles), indicating incomplete phosphorization of the CoOx precursor. The lattice fringes of 0.186 nm and 0.280 nm belong to the (211) and (011) crystal planes of CoP, respectively. Additionally, the diffraction spots in the selected area electron diffraction (SAED) in Fig. S3c† also demonstrate the emergence of crystalline CoP (Area I) and amorphous CoOx (Area II).

It is apparent from Fig. 2a and b that the as-prepared CoOx/CoP-L well maintains the ultrathin nanosheet structure, indi-

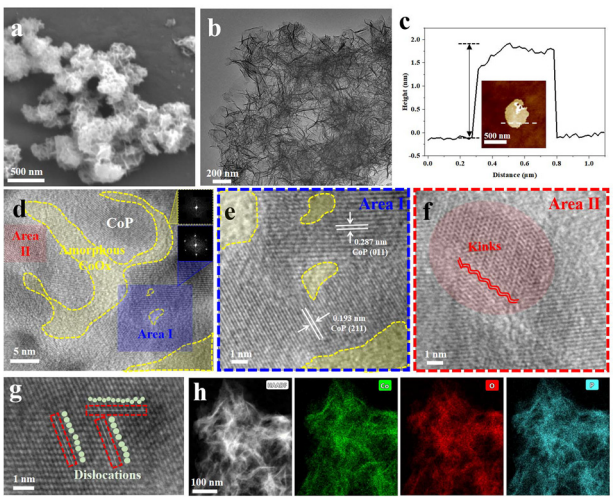

Fig. 2 Physical characterization of CoOx/CoP-L: (a) SEM image, (b) TEM image, (c) thickness measurement diagram (inset: the atomic force microscope image), (d–f) HRTEM images (the illustration inside Fig. 1d is the selected area electron diffraction image), (g) ACTEM image and (h) TEM mapping images.

cating that the quenching treatment has no destructive effect on the nanosheet structure. However, Fig. 2c shows that the thickness of the CoOx/CoP-L nanosheets is similar to that of CoOx/CoP, which is about 2 nm, disclosing that the phosphatization process thickens the nanosheets. Similarly, its HRTEM image (Fig. 2d) displays that CoOx/CoP-L consists of crystalline CoP and amorphous CoOx (marked by yellow dashed circles). Notably, the related SAED patterns of crystalline CoP and amorphous CoOx also proved the formation of amorphous/crystalline (a/c)-heterostructures (Fig. S5a–b†). In particular, the presence of the a/c-heterointerface provides a bridge for electron migration and lays the foundation for optimizing the electronic structure of CoP species. Moreover, the amorphous CoOx phase can expose more unsaturated sites for improving catalyst activity. Further analysis of region I (Fig. 2e) finds that the lattice spacings belonging to the (211) and (011) lattice planes of CoP increase to 0.193 nm and 0.287 nm, respectively. This lattice expansion phenomenon confirms that the quenching treatment induces tensile strain in the CoP crystal. Interestingly, the lattice of CoP exhibits obvious kinks (marked by a red shadow) in region II (Fig. 2f). This is because the newly-formed CoP species, created in a thermodynamically non-equilibrium state, are rapidly cooled during the quenching process. As a result, some active Co and P atoms are instantly immobilized in place rather than arranging themselves according to the normal crystal structure. Strikingly, the high-angle annular dark-field scanning electron microscope (HAADF-STEM) image in Fig. 2g displays that there are obvious dislocations in the CoP crystal, further confirming that a plunge in temperature has a great influence on the crystal structure and atomic arrangement of phosphide. Moreover, the corresponding elemental energy dispersive X-ray (EDX-mapping) images (Fig. 2h) prove that the Co, O, and P elements in the well-designed CoOx/CoP-L ultrathin nanosheets are uniformly distributed.

To further explore the effect of quenching on the strain structure and electronic configuration of CoOx/CoP-L, the strain structure, chemical composition, and bonding state were analyzed using geometric phase analysis (GPA), X-ray diffraction (XRD) and X-ray photoelectron spectroscopy (XPS). Notably, GPA is considered an intuitive method for determining the strain type and strain value. Fig. S6 and S7† show that the CoP crystal of CoOx/CoP-L has an obvious tensile strain, and the tensile strain value is as high as 2.65%, while the tensile strain value of CoOx/CoP without quenching is very low (0.11%) and can be ignored. This phenomenon further confirms the important regulation effect of quenching treatment on the strain structure of CoP. As can be observed in Fig. 3a, both CoOx/CoP and CoOx/CoP-L have a large broad peak corresponding to amorphous CoOx, along with sharp diffraction peaks assigned to the CoP phase (PDF# 29-0497). This implies that the amorphous CoOx is partially transformed into CoP crystals after gas-phase phosphorization. However, the peaks corresponding to CoP in CoOx/CoP-L slightly shift to a smaller angle, indicating that the quenching treatment leads to expansion of the CoP lattice. This result is consistent with

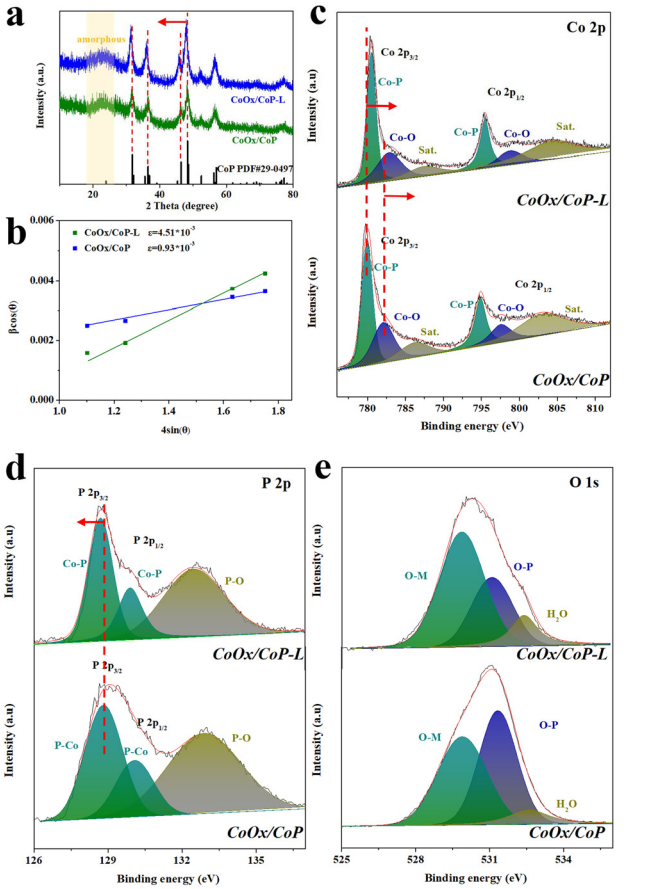

Fig. 3 (a) XRD patterns of CoOx/CoP and CoOx/CoP-L, (b) the tensile strain coefficient diagram obtained by XRD fitting, (c–e) XPS spectra of CoOx/CoP and CoOx/CoP-L.

the phenomenon in Fig. 2e, disclosing that quenching treatment induces tensile strain in CoP. In addition, the lattice strain was investigated by Williamson–Hall (W–H) analysis. As shown in Fig. 3b, CoOx/CoP-L exhibits a significantly higher strain (ε) value (4.51×10^{-3}) compared to CoOx/CoP (0.93×10^{-3}), further revealing that the tensile strain induced by the quenching treatment aligns well with the negative shift of the CoP peaks in Fig. 3a. Moreover, in Fig. 3c, CoOx/CoP-L displays three pairs of peaks. A pair of peaks located at 780.54 eV and 795.53 eV are assigned to the Co–P species, indicating the formation of the CoP phase. The peaks at 782.92 eV and 798.93 eV belong to Co–O bonds, implying the presence of amorphous CoOx. In the P 2p spectrum (Fig. 3d), the peaks located at 129.44 eV and 130.52 eV are ascribed to P–Co bonds, confirming the presence of the CoP phase. The peak at 133.49 eV corresponds to P–O bonds. Moreover, the O 1s spectrum in Fig. 3e decomposes into three peaks at 529.89 eV, 531.35 eV, and 531.9 eV, corresponding to O–Co bonds, O–P bonds, and H_2O, respectively. The peak corresponding to O–Co bonds indicates the presence of amorphous CoOx. Notably, compared with the ordinary CoOx/CoP catalyst, both Co–P and Co–O species in the Co 2p spectrum of CoOx/CoP-L shift toward

higher binding energy, implying that Co atoms in CoOx/CoP-L carry more positive charges under the action of lattice tensile strain. In contrast, the peaks belonging to the P–Co species in CoOx/CoP-L have a reverse shift, indicating that the lattice strain induced by quenching treatment causes P sites to have more electrons.

In summary, the introduction of a strained structure effectively promotes the electron reset of CoOx/CoP-L. Interestingly, the decrease in the P–O bond content for CoOx/CoP-L suggests that the N_2 volatilized during the liquid nitrogen quenching process inhibits the peroxidation of the phosphides and effectively protects the CoP active species.

Considering the structural superiorities of the CoOx/CoP-L nanosheets, the HER performances of CoOx/CoP-L and other counterparts were monitored in 1.0 M KOH solution. As can be observed in Fig. 4a, the overpotentials of CoOx/CoP-L and CoOx/CoP electrocatalysts with a/c-heterostructures at the same current density are significantly superior to those of their amorphous CoOx counterparts, indicating that integration of crystalline CoP and amorphous CoOx drastically enhances the alkaline HER activity. Surprisingly, the alkaline HER activity of CoOx/CoP-L begins to exceed that of Pt/C at a current density of 68 mA cm^{-2}.

As shown in Fig. 4b and Table S4,† the overpotentials of CoOx/CoP-L at current densities of 50, and 100 mA cm^{-2} are 106.4 mV, and 128.1 mV, respectively, which are much lower than those of CoOx/CoP without quick-freezing treatment (127.4 mV and 149.6 mV), or commercial Pt/C (101.6 mV and 134.2 mV). It is noteworthy that the ultrahigh alkaline HER activity of CoOx/CoP-L arises mainly from the local strain effect on the CoP crystals induced by the rapid freezing treatment. Moreover, the Tafel slope of CoOx/CoP-L (63.2 mV dec^{-1}) is also close to that of commercial Pt/C (61.9 mV dec^{-1})

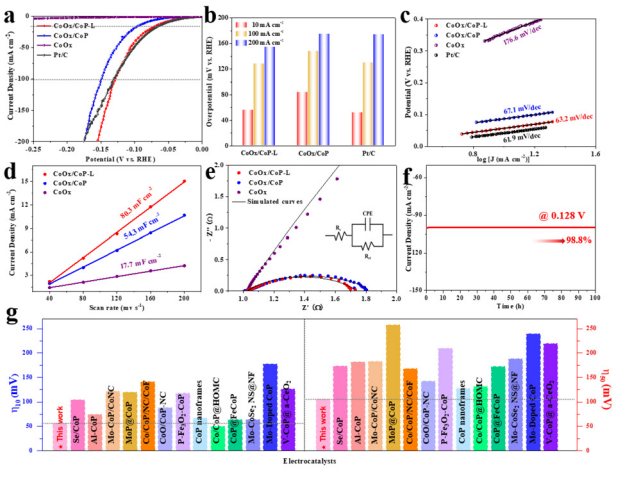

Fig. 4 HER electrocatalytic properties of CoOx/CoP, CoOx/CoP-L, CoOx precursor and Pt/C in 1.0 M KOH: (a) LSV curves, (b) comparison diagram of voltage at current densities of 10, 100, and 200 mA cm^{-2}, (c) Tafel slopes, (d) C_{dl} curves, (e) Nyquist plots at a specific voltage of −0.15 V, (f) chronoamperometry test of CoOx/CoP-L and (g) comparison diagram of recently reported Co-based electrocatalysts.

in Fig. 4c, showing that CoOx/CoP-L possesses exceptional alkaline HER kinetics. The electrochemical surface area (ECSA) is a vital indicator to reveal the intrinsic activity of catalysts. Generally, the electric double-layer capacitance (C_{dl}) obtained from the cyclic voltammetry (CV) test (in Fig. S8 and Table S5†) is proportional to the value of ECSA. Fig. 4d demonstrates that the C_{dl} value of CoOx/CoP-L is 80.3 mF cm^{-2}, which is considerably larger than those of CoOx/CoP (54.3 mF cm^{-2}) or CoOx (17.7 mF cm^{-2}). This result means that CoOx/Co P-L exposes abundant electrocatalytically active sites, which is closely related to the lattice strain (tensile strain, lattice distortion, dislocation) of CoP crystals. In conclusion, the strain structure in CoP crystals significantly contributes to the exposure of the active sites. Moreover, the electrochemical impedance spectroscopy (EIS) in Fig. 4e and Table S6† reveals that CoOx/CoP-L has the smallest charge transfer resistance (R_{ct}) among all the as-prepared catalysts, suggesting that the lattice strain of CoP crystals promotes the conductivity of the material to a certain extent. Except for electrochemical activity, stability is a vital indicator for describing the industrial-scale application of catalysts. As can be seen in Fig. 4f, CoOx/CoP-L maintains a stable current density of 100 mA cm^{-2} for 100 h under a constant potential of 0.106 V. To further investigate its durability of composition and structure after the alkaline HER test, XPS and TEM characterizations were conducted. Fig. S9† displays that there is no change in the XPS spectrum of CoOx/CoP-L after the HER test. Meanwhile, the TEM and HRTEM images of CoOx/CoP-L (in Fig. S10†) after HER show that the nanosheet morphology and the strain structure of CoP are well maintained. Overall, the above characterizations confirm the remarkable durability of CoOx/CoP-L in terms of physical structure, chemical composition and HER performance. In particular, the strain structure stabilized in CoP crystals plays an important role in the stable and efficient HER process of CoOx/CoP-L. Significantly, the HER activity of the CoOx/CoP-L nanosheets exceeds that of the most commonly reported non-noble–metal-based catalysts (Fig. 4g and Table S7†), further verifying that the lattice strain and the a/c-CoOx/CoP heterostructures jointly promote the improvement in HER performance.

Surprisingly, Fig. 5a shows that CoOx/CoP-L also exhibits excellent HER activity with an ultra-low η_{10} of 85.6 mV in 0.5 M H_2SO_4, benefiting from the presence of a/c-CoOx/CoP heterostructures and lattice strain (tensile strain, lattice distortion, dislocation). Notably, although the acidic HER performances of CoOx/CoP-L in Fig. 5b and Table S8† are still far from those of Pt/C, only 85.6 mV, 138.4 mV, and 163.6 mV are required to achieve current densities of 10, 50, and 100 mA cm^{-2}, which are significantly lower than those of CoOx/CoP (117.4 mV, 169.2 mV, and 195.6 mV), revealing the significance of the lattice strain induced by the quick-freezing treatment. Meanwhile, Fig. 5c demonstrates that CoOx/CoP-L shows expedited acidic HER kinetics. The C_{dl} value demonstrates the huge ECSA of CoOx/CoP-L (Fig. S11,† Fig. 5d, and Table S9†), suggesting that the lattice strain inside the CoP crystal effectively promotes the exposure of abundant active sites. The

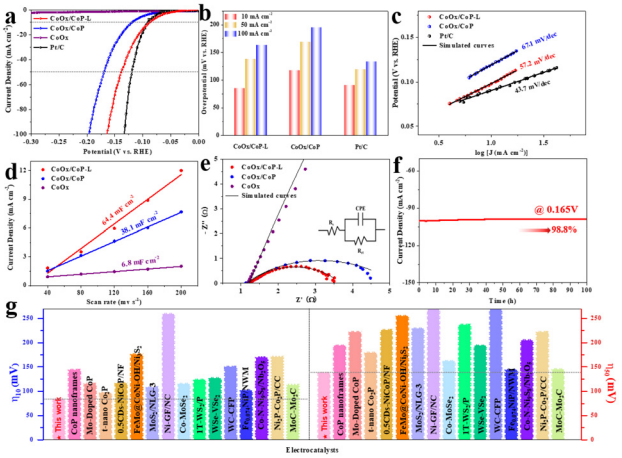

Fig. 5 HER electrocatalytic properties of CoOx/CoP, CoOx/CoP-L, CoOx precursor and Pt/C in 0.5 M H_2SO_4: (a) LSV curves, (b) comparison diagram of voltage at current densities of 10, 50, and 100 mA cm^{-2}, (c) Tafel slopes, (d) C_{dl} curves, (e) Nyquist plots at a specific voltage of −0.15 V, (f) chronoamperometry test of CoOx/CoP-L and (g) comparison diagram of recently reported non-noble–metal-based electrocatalysts.

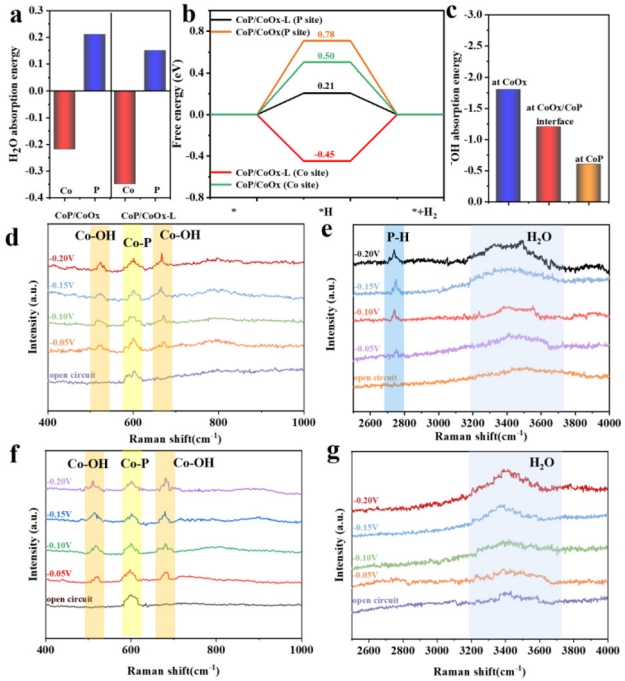

Fig. 6 (a) H_2O absorption capacity of site at CoOx/CoP and CoOx/CoP-L, (b) calculated free energy diagrams of H*, (c) OH^- absorption capacity of Co site at different positions in the CoOx/CoP-L model; *in situ* Raman spectra of (d and e) CoOx/CoP-L and (f and g) CoOx/CoP in the alkaline HER process.

tensile strain and appropriate dislocation of CoOx/CoP-L induced by the quenching treatment can promote more exposure of active sites, thereby achieving a larger electrochemically active area. Fig. 5e and Table S10† reveal the excellent conductivity of CoOx/CoP-L. In addition, the *I*–*T* test in Fig. 5f confirms the outstanding electrochemical stability of CoOx/CoP-L under acidic conditions. Surprisingly, as exhibited in Fig. S12,† the morphology of CoOx/CoP-L hardly changes after an acidic HER test, and the lattice strain region still exists in the CoP region. At the same time, the differences in the XPS spectra of Co, P, and O (Fig. S13†) are also negligible, revealing the superior durability of CoOx/CoP-L in terms of chemical composition. Additionally, the acidic HER activity of CoOx/CoP-L is also preeminent compared to most reported non-precious-metal-based catalysts and self-supported electrodes (Fig. 5g and Table S11†). As expected, CoOx/CoP-L also has excellent neutral HER performance (Fig. S14†), indicating that CoOx/CoP-L has excellent hydrogen evolution ability in all pH ranges, making it suitable for all electrolytic cells.

To comprehensively reveal the HER catalytic mechanism of CoP/CoOx-L, in-depth DFT calculations on different active sites of CoP/CoOx-L were performed. Fig. 6a and Table S12† show that the Co sites at the a/c-CoP/CoOx heterointerface in the CoP/CoOx-L and CoP/CoOx models have better water adsorption capacity than the P sites, confirming the Co site at the a/c-CoP/CoOx heterointerface as the main hydrophilic site. Furthermore, the adsorption energy of H_2O at Co sites in the CoP/CoOx-L model was much better than that in the CoP/CoOx model, indicating that the 2.65% tensile strain further optimizes the hydrophilicity. As can be seen in Fig. 6b and Table S13,† the H* adsorption sites of the CoP/CoOx model are still Co sites at the a/c-CoP/CoOx heterointerface, consistent with the hydrophilic sites. However, the H* adsorption site of the CoP/CoOx-L model changes to a P site at the heterointerface, suggesting that water adsorption and hydrogen desorption in the tensile-strain-driven CoP/CoOx-L model occur at the Co site and the P site at the heterointerface, respectively. Moreover, the $|\Delta G_{H^*}|$ value of the P site in the CoP/CoOx-L model is much lower than that of the Co site in the CoP/CoOx model, confirming that tensile strain induces a transition of the H* adsorption site to achieve a sudden drop in the energy barrier to hydrogen evolution. Strikingly, OH^- produced by water-splitting during alkaline HER is severely toxic to the hydrophilic sites. Therefore, it is vital to optimize the OH^- adsorption path. Fig. 6c and Table S14† demonstrate the OH^- adsorption capacity on Co sites at different positions in the CoP/CoOx-L model. Surprisingly, a Co site located in amorphous CoOx has much better OH^- adsorption ability than that at the a/c-heterointerface. The above results reveal that the Co site located at the a/c-heterointerface in the CoP/CoOx-L model dissociates water molecules as a hydrophilic site during alkaline HER. The H^+ and OH^- formed by water dissociation are then spontaneously transferred to the P site at the a/c-heterointerface and the Co site at the amorphous CoOx, respectively. This unique Co_1–P–Co_2 catalytic mechanism for alkaline HER avoids poisoning of the Co_1 hydrophilic site, thus achieving a great enhancement in alkaline HER kinetics. To further corroborate the unique Co_1–P–Co_2 mechanism of the CoP/CoOx-L model for alkaline HER, *in situ* Raman testing of CoP/

CoOx-L and CoP/CoOx was performed. Fig. 6d–f show that the peaks belonging to Co–P bonds are almost unchanged during alkaline HER for both CoP/CoOx-L and CoP/CoOx, implying that the Co–P species of CoP/CoOx and CoP/CoOx-L are stable during the alkaline HER process. Surprisingly, with increasing voltage, the intensity of the Co–OH peaks strengthens significantly in CoP/CoOx-L and CoP/CoOx, further proving that the OH^- formed by dissociation of water is transferred to the CoOx phase of CoP/CoOx and CoP/CoOx-L to form Co–OH species. As shown in Fig. 6e, as the voltage increases, a continuously enhanced peak attributed to the P–H bond appears at 2690 cm^{-1} for CoP/CoOx-L, indicating that the P atom in CoP/CoOx-L is the active site for *H adsorption. However, Fig. 6g shows that there is no peak belonging to the P–H bond in CoP/CoOx during the alkaline HER process, indicating that the *H adsorption site in CoP/CoOx has always been the Co site, which is consistent with the DFT calculation results. In conclusion, the above results confirm that the tensile strain induces a change in the *H adsorption site in CoP/CoOx-L. Notably, CoP/CoOx-L follows a unique Co_1–P–Co_2 electrocatalytic mechanism in the alkaline HER process. The simultaneous transfer of H^+ and OH^- intermediates effectively avoids poisoning of the hydrophilic site, thereby enhancing the alkaline HER kinetics.

To further explore the effect of quick-freezing temperature on crystal structure and electrocatalytic performance, the material in this work was quenched using Drikold (−79 °C) and ice water (0 °C) to prepare CoOx/CoP-D and CoOx/CoP-I comparison samples, respectively. As shown in Fig. S15a and S16a,† CoOx/CoP-D and CoOx/CoP-I still maintain the morphology of ultrathin nanosheets. The related HRTEM images (Fig. S15b, c and S16b, c†) show that both CoOx/CoP-I and CoOx/CoP-D nanosheets are composed of amorphous and crystalline regions. The lattice stripes in their crystalline regions all belong to the CoP phase, but there are different degrees of lattice expansion. As the freezing temperature decreases, the lattice spacing belonging to the same crystal faces of the CoP phase tends to increase, indicating that the tensile strain in CoP is also gradually increasing. Notably, the CoP phase in CoOx/CoP-I has the smallest lattice expansion and its lattice remains free of kinks. Although CoOx/CoP-D has similar lattice kink regions to CoOx/CoP-L, its lattice expansion is lower than that of CoOx/CoP-L. Simultaneously, the related GPA test (Fig. S17 and 18†) confirms that the tensile strain of CoP in CoOx/CoP-I (1.05%) is much lower than those of CoOx/CoP-D (1.85%) or CoOx/CoP-L (2.65%). Above all, the quick-freezing treatment causes tensile strain in the CoP lattice, and the degree of the tensile strain is inversely proportional to the quick-freezing temperature.

In a traditional three-electrode system, the alkaline/acid HER activities of catalysts obtained by three different quick-freezing methods were determined from LSV and Tafel curves. As can be seen in Fig. S19 and S20,† CoOx/CoP-L shows distinct superiority over CoOx/CoP-I and CoOx/CoP-D in terms of alkaline HER performance and acid HER performance, confirming that the appropriate lattice tensile strain can greatly accelerate HER kinetics. Above all, the huge temperature difference brought about by the lower quenching temperature induces a larger tensile strain of the CoP crystals, regulating the electronic structure and optimizing the intrinsic activity of the active sites.

In addition, the amorphous/crystalline ratio in CoOx/CoP-*X*-L (*X* = 10, 50) was also regulated by adjusting the feeding ratio of CoOx to sodium hypophosphite (specifically, the feeding ratios were 10 and 50) during phosphorization. Strikingly, as can be seen in Fig. S21a and S22a,† the CoOx/CoP-*X*-L (*X* = 10, 50) counterparts also have the structure of ultrathin nanosheets, implying that the degree of phosphorization has little effect on the morphology of CoOx/CoP-*X*-L. However, Fig. S21b† shows that CoOx/CoP-10-L contains abundant amorphous CoOx regions, indicating that insufficient P source is not conducive to the formation of phosphide. As can be seen in Fig. S22b,† when the feed ratio is as high as 50, amorphous CoOx is almost completely converted into CoP crystals due to excessive phosphorization. Simultaneously, a distorted lattice is also observed in the CoP phase of CoOx/CoP-10-L and CoOx/CoP-50-L (Fig. S21c and S22c†), implying the presence of tensile strain induced by quenching treatment. The XPS spectra of CoOx/CoP-*X* and CoOx/CoP-*X*-L (*X* = 10, 50) are shown in Fig. S23.† Moreover, according to the peak area ratio of Co–P and Co–O bonds in the Co 2p spectra of CoOx/CoP-*X* and CoOx/CoP-*X*-L (*X* = 10, 50), the relative content of Co–P and Co–O bonds was calculated. Obviously, with an increase in *X* value, the content of Co–P bonds in CoOx/CoP-*X*-L increases, while the content of Co–O bonds decreases. This phenomenon further confirms that increasing the P source can promote the transformation of amorphous CoOx into CoP crystals. Furthermore, an alkaline HER test was carried out on CoOx/CoP-L and CoOx/CoP-*X*-L (*X* = 10 and 50). The LSV curves (in Fig. S24†) display that CoOx/CoP-30 has the best electrochemical activity and the lowest Tafel slope among them. As expected, acidic HER showed similarly excellent activity (Fig. S25†). These results indicate that the appropriate phosphorization optimizes the content ratio of amorphous CoOx to CoP crystal, thereby stimulating its superior electrocatalytic activity. Fig. S26 and S27† confirm that CoOx/CoP-L maintains the best HER property in both alkaline and acidic media. At the same time, these catalysts show optimized HER activity after quick-freezing treatment, indirectly confirming the universality of quick-freezing treatment for the improvement of properties in this system.

4. Conclusions

In summary, a facile 'phosphorization–liquid nitrogen quenching' method was used to construct well-designed CoOx/CoP-L heterostructure nanosheets consisting of amorphous CoOx and crystalline CoP with 2.65% tensile strain. As anticipated, the CoOx/CoP-L nanosheets require ultra-low overpotentials of only 128.1 mV and 163.6 mV to drive 100 mA cm^{-2} for alkaline and acidic HER, which is significantly better than most devel-

oped non-noble–metal-based catalysts. Remarkably, it also achieves excellent HER stability and has commendable value in industrial applications. DFT calculations and *in situ* Raman results confirm that the construction of the a/c-CoOx/CoP heterostructure with 2.65% tensile strain optimizes the energy barrier to adsorption of H^+ for acid HER and water adsorption–dissociation for alkaline HER. Strikingly, a unique Co_1–P–Co_2 electrocatalytic pathway for alkaline HER is innovatively proposed in the a/c-CoOx/CoP heterostructure with 2.65% tensile strain. Among the sites, the Co_1 site at the a/c-heterointerface and the Co_2 site at the amorphous CoOx are a hydrophilic site and a site for the adsorption of OH^-, respectively, effectively avoiding poisoning of the hydrophilic site and accelerating the alkaline HER kinetics. This work creatively stimulated the a/c-heterostructure and lattice strain structure by quenching during the phosphorization process, providing a novel method for the construction of non-noble–metal phosphide catalysts with a performance surpassing that of Pt for HER.

Author contributions

Yunmei Du: Conceptualization, formal analysis, data curation. Jinghan Xu: Investigation, writing – original draft. Shan Lu: Formal analysis, visualization. Zhenyu Xiao: Methodology, formal analysis. Yanru Liu: Investigation, formal analysis, resources. Kang Liu: Validation, formal analysis. Lei Wang: Validation, formal analysis, resources.

Conflicts of interest

The authors declare that they have no known competing financial interests or personal relationships that could have appeared to influence the work reported in this paper.

Data availability

The data supporting this article have been included as part of the ESI.†

Acknowledgements

This work was supported by the National Natural Science Foundation of China (52302274, 52072197), Natural Science Foundation of Shandong Province, China (ZR2022QE098), the 111 Project of China (Grant No. D20017), Youth innovation team of colleges and universities in Shandong Province (2023KJ313), Postdoctoral Innovation Project of Shandong Province (SDCX-ZG-202203075), Double-Hundred Talent Plan of Shandong Province (WST2020003). The authors would like to thank Songhe Zhang from SCl-Go (**https://www.sci-go.com**) for the DFT analysis.

References

1 W. Zhu, W. Hu, Y. Wei, Y. Zhang, K. Pan, S. Zhang, X. Hang, M. Zheng and H. Pang, Core-Shell Co-CoxP Nanoparticle-Embedded N-Doped Carbon Nanowhiskers Hollow Sphere for Efficient Oxygen Evolution Electrocatalysis, *Adv. Funct. Mater.*, 2024, 202409390.
2 G. Y. Jang, S. Kim, J. Choi, J. Park, S. An, J. Baek, Y. Li, T. Liu, E. Kim, J. H. Lee, H. Wang, M. Kim, H. Cho, X. Zheng, J. S. Yoo, K. Seo and J. H. Park, Bulk-Heterojunction Electrocatalysts in Confined Geometry Boosting Stable, Acid/Alkaline-Universal Water Electrolysis, *Adv. Energy Mater.*, 2024, **14**, 2303924.
3 C. Luo, X. Liu, K. Yang, J. Xu, Z. Zhu, Z. Tang, S. Shen, J. Fan, D. Luo, N. A. H. Alshammari, Z. M. El-Bahy, X. Xu, Y. Xue and L. Pan, Coordination structure engineering of Cu-based electrocatalysts for electrocatalytic water splitting, *Coord. Chem. Rev.*, 2024, **516**, 215936.
4 J. Tang, X. Liu, X. Xiong, Q. Zeng, Y. Ji, C. Liu, J. Li, H. Zeng, Y. Dai, X. Zhang, C. Li, H. Peng, Q. Jiang, T. Zheng, C.-W. Pao and C. Xia, Ruthenium Single-Atom Modulated Protonated Iridium Oxide for Acidic Water Oxidation in Proton Exchange Membrane Electrolysers, *Adv. Mater.*, 2024, **36**, 2407394.
5 Y. Chen, Y. Liu, W. Zhai, H. Liu, T. Sakthivel, S. Guo and Z. Dai, Metastabilizing the Ruthenium Clusters by Interfacial Oxygen Vacancies for Boosted Water Splitting Electrocatalysis, *Adv. Energy Mater.*, 2024, **14**, 2400059.
6 H. Xu, K. Wang, G. He and H. Chen, Concurrent alloying and vacancy engineering for intensifying hydrogen spillover towards alcohol-water co-electrolysis, *J. Mater. Chem. A*, 2023, **11**, 17609–17615.
7 J. Kim, J. Oh, S. Baskaran, T. G. Kim, S. Kim, J. Yang, J. Jung and S. M. Yoon, Rhenium redefined as electrocatalyst: Hydrogen evolution efficiency boost via Pt and Ni doping, *Appl. Catal., B*, 2024, **347**, 123791.
8 H. Yoon, H. Song, J. Hyoung, S. Jung, A. Haryanto, C. Lee and D. Kim, Facet-engineered ruthenium oxide on titanium oxide oxygen evolution electrocatalysts for proton-exchange membrane water electrolysis, *Appl. Catal., B*, 2024, **358**, 124382.
9 T. Zhu, C. Xia, B. Wu, J. Pan, H. Yang, W. Zhang and B. Y. Xia, Inbuilt photoelectric field of heterostructured cobalt/iron oxides promotes oxygen electrocatalysis for high-energy-efficiency zinc-air batteries, *Appl. Catal., B*, 2024, **357**, 124315.
10 Y. Li, Z. Zhang, C. Li, Y. Zhou, X.-B. Chen, H. Lu, Z. Shi and S. Feng, Introducing phosphorus into spinel nickel ferrite to enhance lattice oxygen participation towards water oxidation electrocatalysis, *Appl. Catal., B*, 2024, **355**, 124116.
11 S. Zhang, M. Jin, H. Xu, X. Zhang, T. Shi, Y. Ye, Y. Lin, L. Zheng, G. Wang, Y. Zhang, H. Yin, H. Zhang and H. Zhao, An oxygen-coordinated cobalt single-atom electrocatalyst boosting urea and urea peroxide production, *Energy Environ. Sci.*, 2024, **17**, 1950–1960.
12 H. Xu, Y. Liu, K. Wang, L. Jin, J. Chen, H. Chen and G. He, High-entropy layered double hydroxides tailor Pt electron

state for promoting acidic hydrogen evolution reaction, *J. Colloid Interface Sci.*, 2025, **684**, 566–574.

13 Z. Niu, S. Fan, X. Li and G. Chen, Electrocatalytic Co-Upcycling of Nitrite and Ethylene Glycol over Cobalt-Copper Oxides, *Adv. Energy Mater.*, 2024, **14**, 2303515.

14 R. Wu, Q. Meng, J. Yan, Z. Zhang, B. Chen, H. Liu, J. Tai, G. Zhang, L. Zheng, J. Zhang and B. Han, Intermetallic synergy in platinum-cobalt electrocatalysts for selective C-O bond cleavage, *Nat. Catal.*, 2024, **7**, 702–718.

15 L. Jin, H. Xu, K. Wang, Y. Liu, X. Qian, H. Chen and G. He, Modulating built-in electric field via Br induced partial phase transition for robust alkaline freshwater and seawater electrolysis, *Chem. Sci.*, 2025, **16**, 329–337.

16 E. Mijowska, A. Dymerska, G. Leniec, K. Maślana, M. Aleksandrzak, R. Zairov, R. Nazmutdinov and X. Chen, Ni-based compounds in multiwalled graphitic shell for electrocatalytic oxygen evolution reactions, *Adv. Compos. Hybrid Mater.*, 2024, **7**, 172.

17 C. Wang, W. Guo, T. Chen, W. Lu, Z. Song, C. Yan, Y. Feng, F. Gao, X. Zhang, Y. Rao, L. Qian, S. Xu, G. Huang, Y. Zheng, W. Yan and J. Zhang, Advanced noble-metal/transition-metal/metal-free electrocatalysts for hydrogen evolution reaction in water-electrolysis for hydrogen production, *Coord. Chem. Rev.*, 2024, **514**, 215899.

18 Z. Feng, H. Meng, Y. Fu, L. Ren, B. Gao and W. Liu, Modulation of Charge Redistribution in Heterogeneous CoSe-$Ni_{0.95}Se$ Coupling with $Ti_3C_2T_x$ MXene for Hydrazine-Assisted Water Splitting, *Small*, 2024, **20**, 202403270.

19 R.-L. Chai, Q. Zhao, J. Li, Z.-J. Dong, Y.-X. Sun, X. Wang, P. Zhang, W.-T. Wu, G.-Y. Li, J. Zhao and S.-H. Li, Superior Oxygen Evolution Electrocatalyst based on Ni-Ellagic Acid Coordination Polymer, *Adv. Energy Mater.*, 2024, **14**, 2400871.

20 T. Shi, B. Gao, H. Meng, Y. Fu, D. Kong, P. Ren, H. Fu and Z. Feng, In situ electronic redistribution of NiCoZnP/NF heterostructure via Fe-doping for boosting hydrazine oxidation and hydrogen evolution, *Green Chem.*, 2024, **26**(7), 4209–4220.

21 X. Ding, D. Liu, P. Zhao, X. Chen, H. Wang, F. E. Oropeza, G. Gorni, M. Barawi, M. García-Tecedor, V. O'Shea, J. P. Hofmann, J. Li, J. Kim, S. Cho, R. Wu and K. Zhang, Dynamic restructuring of nickel sulfides for electrocatalytic hydrogen evolution reaction, *Nat. Commun.*, 2024, **15**, 5336.

22 W. Liu, T. Shi and Z. Feng, Bifunctional zeolitic imidazolate framework-67 coupling with CoNiSe electrocatalyst for efficient hydrazine-assisted water splitting, *J. Colloid Interface Sci.*, 2023, **630**, 888–899.

23 Y. Fu, H. Liu, B. Gao, J. Mu, G. Guan and Z. Feng, High-entropy $(FeMnMoNi)Se_2$ nanoflower structure with multi-active sites for urea-assisted hydrogen generation, *Chem. Eng. J.*, 2025, **511**, 162264.

24 Z. Yuan, X. Sun, B. Gao, Z. Fan, P. Yang and Z. Feng, Regulating the electronic structure of Ni_3Se_4-$MoSe_2$ by coupling with ZIF-derived Co@C promotes boosted urea-assisted water splitting at industrial current density, *Chem. Eng. J.*, 2024, **499**, 156647.

25 X. Chen, Y. Du, Y. Yang, K. Liu, J. Zhao, X. Xia and L. Wang, Quenching to optimize the crystalline/amorphous ratio of CoPS nanorods for hydrazine-assisted total water decomposition at ampere-level current density, *Chin. J. Catal.*, 2024, **62**, 265–276.

26 J. D. Rodney, S. Joshi, S. Ray, L. Rao, S. Deepapriya, K. Carva, B. R. Bhat, N. K. Udayashankar, S. Perumal, S. Katlakunta, C. J. Raj and B. C. Kim, Electrocatalytic synergies of melt-quenched Ni-Sn-Se-Te nanoalloy for direct seawater electrolysis, *Chem. Eng. J.*, 2024, **499**, 155775.

27 B. Huang, Y. Liu, Q. Pang, *et al.*, Boosting the photocatalytic activity of mesoporous SrTiO3 for nitrogen fixation through multiple defects and strain engineering, *J. Mater. Chem. A*, 2020, **8**(42), 22251–22256.

28 J. Baek, M. D. Hossain, P. Mukherjee, J. Lee, K. T. Winther, J. Leem, Y. Jiang, W. C. Chueh, M. Bajdich and X. Zheng, Synergistic effects of mixing and strain in high entropy spinel oxides for oxygen evolution reaction, *Nat. Commun.*, 2023, **14**, 5936.

29 J. Li, L. Li, J. Wang, A. Cabot and Y. Zhu, Boosting Hydrogen Evolution by Methanol Oxidation Reaction on Ni-Based Electrocatalysts: From Fundamental Electrochemistry to Perspectives, *ACS Energy Lett.*, 2024, **9**, 853–879.

30 A. Naderi, M. Jourshabani, M. R. Asrami and B.-K. Lee, Bottom-up reconstruction and phase change over nickel–iron layered double hydroxides for boosted electrocatalytic oxygen evolution reaction, *Chem. Eng. J.*, 2024, **484**, 149111.

31 S.-W. Yu, S. Kwon, Y. Chen, Z. Xie, X. Lu, K. He, S. Hwang, J. G. Chen, W. A. Goddard and S. Zhang, Construction of a Pt-CeOx Interface for the Electrocatalytic Hydrogen Evolution Reaction, *Adv. Funct. Mater.*, 2024, **34**, 2402966.

32 Y. Shi, M. Wang, D. Zhang, H. Li, C. Li, T. Zhan, J. Lai and L. Wang, Atomically Dispersed Interstitial Phosphorus Boosts Alkaline Hydrogen Evolution Performance of Co Catalysts, *Adv. Funct. Mater.*, 2024, 2410825.

33 C. Zhao, Y. Huang, B. Jiang, Z. Chen, X. Yu, X. Sun, H. Zhou, Y. Zhang and N. Zhang, The Origin of Strain Effects on Sulfur Redox Electrocatalyst for Lithium Sulfur Batteries, *Adv. Energy Mater.*, 2024, **14**, 2302586.

34 Z. Gao, J.-H. Liu, S. Wang, W. Yang, W. Wang, L. Li, H. Guo, J. Zheng, S. Ramakrishna, J. Zhang, L. Yang and Y.-Z. Long, Quenching controlled spin exchange interactions and spin selective electron transfer for oxygen evolution reactions, *Chem. Eng. J.*, 2024, **496**, 154216.

35 X. Wang, X. Yin, P. Sun, L. Tang, Y. Tong, X. Li, X. Gao, X. Chen and X. Ma, Vapor-phase quenching synthesis of atomically dispersed PtMn alloy clusters for anti-CO hydrogen oxidation electrocatalysis, *Chem. Eng. J.*, 2024, **498**, 155556.